Available online at www.sciencedirect.com

ScienceDirect

journal homepage: www.elsevier.com/locate/he

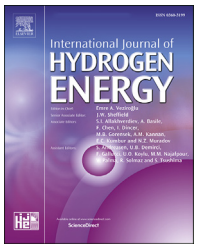

Investigating the pressure loss associated with two-phase flow in a rectangular microchannel suddenly expanding into a manifold

*James M. Lewis, Yun Wang**

Renewable Energy Resources Laboratory, National Fuel Cell Research Center and Department of Mechanical and Aerospace Engineering, University of California, Irvine, CA, USA

ARTICLE INFO

Article history:
Received 8 May 2018
Received in revised form
3 July 2018
Accepted 16 July 2018
Available online 9 August 2018

Keywords:
Two-phase flow
Microchannel
Sudden expansion
90-degree bend
Exit effects

ABSTRACT

This study focuses on the experimental investigation of the two-phase pressure loss occurring as air-water flow exits a microchannel to a larger manifold. The microchannel has dimensions of 3.23 mm wide by 0.304 mm high by 164 mm long and expands into an exit manifold of 1.4 cm diameter oriented 90° relative to the flow direction. The expansion results in an additional 150–400 Pa pressure loss. Visualization of the flow illustrates water accumulation at the channel exit with varying behavior, resulting in the range of the pressure loss. Using the sudden expansion model of Abdelall et al. resulted in a mean absolute percent error of 96%. Treating the pressure loss as a result of the 90° bend, the model of Paliwoda produced a mean absolute percent error of 81%. The combined influence of the models of Abdelall et al. and Paliwoda predicted the experimental measurement with a mean absolute percent error of 78%.

Introduction

Pipe systems inevitably include bends, area contractions/expansions, or other geometric features that produce minor pressure losses in addition to the major frictional pressure drop. The prediction of the frictional pressure drop of two-phase flows in microchannels has received significant attention in the form of homogeneous [1–6], separated [7–18], and two-fluid models [4,19–24]. However, the minor pressure losses associated with two-phase flow have received less attention. The prevalence of micro-scale devices utilizing two-phase flow and experimental constraints to investigate two-phase frictional pressure loss necessitates an investigation of minor pressure losses.

Micro-heat exchangers present one such micro-scale device. Typically micro-heat exchangers consist of multiple parallel micro-scale channels terminating in an exit manifold of larger scale [25,26]. The coolant flowing through the microchannels undergoes a phase change and thus increases the heat transfer due to the laten heat of vaporization [15,27]. However, the full conversion of the coolant to vapor leads to a condition of dry-out, decreasing the overall heat transfer coefficient [28]. Therefore, designs will seek to maintain two-phase flow throughout the channel. A minor two-phase pressure loss occurs for each channel as the flow suddenly expands into the exit manifold. While decreasing the channel dimensions improves heat transfer, the total pressure drop of the system increases [15]; additional pressure losses may

* *Corresponding author.*
E-mail address: yunw@uci.edu (Y. Wang).
https://doi.org/10.1016/j.ijhydene.2018.07.112

Nomenclature

Acronyms

FFT	Fast-Fourier transform
PEM	Polymer-Electrolyte Membrane

Greek Symbols

α	Void fraction [–]
α^*	Aspect ratio (smallest dimension/largest dimension) [–]
α_E	Mean volumetric liquid entrainment for Schmidt & Friedel (1996)
β	Homogeneous void fraction [–]
χ	Gas quality [–]
Δ	Difference between points
δ^*P	Percent error [–]
γ	Contact angle [deg.]
Γ_e	Downstream pressure correction term of Schmidt & Friedel (1996)
κ	Resistance coefficient [–]
μ	Dynamic viscosity [kg/m•s]
ϕ^2	Two-phase flow multiplier [–]
ρ	Density [kg/m^3]
ρ'	Density function (Eq. (36)) of Abdelall et al. (2005)
ρ''	Second density function (Eq. (37)) of Abdelall et al. (2005)
σ	Surface tension [N/m]
σ_A	Area-ratio= A_1/A_2 [–]
Υ	Correlation (Eq. (19)) of Attou & Bolle (1997)
ϑ	Correlation (Eq. (18)) of Attou & Bolle (1997)
X_h	Lockhart-Martinelli parameter [–]

Roman Symbols

$\dot{m}$	Mass flow rate per unit area [kg/m^2·s]
$\frac{R}{D}$	Ratio of bend radius to channel diameter [–]
$\mathbf{n}$	Unit normal [–]
$\mathbf{u}$	Velocity vector [m/s]
$\overline{C}$	Friction correlation constant [–]
$\overline{e}_{\%}$	Mean percent error [–]
A	Area [m^2]
B	Bend Coefficient of Chisholm (1980) [–]
C_h	Chisholm parameter [–]
d	Diameter [m]
D_H	Hydraulic diameter [m]
f	Frication factor [–]
f_m	Syringe pump frequency [Hz]
G	Total mass flux [kg/m^2·s]
g	Acceleration due to gravity [m/S^2]
h	Height [m]
K^*	Correction factor (0.83) of Wadle (1989)
L	Length [m]
n	Number of samples [–]
P	Pressure [Pa]
Q	Volumetric flow rate [m^3/s]
Re	Reynolds number [–]
S	Slip ratio [–]
s	Saturation [–]
U	Superficial velocity [m/s]
u	Axial velocity [m/s]
w	Width [m]
W_{rel}	Relation in the void fraction of Rouhani (1969)
We	Weber number [–]
z	Downstream distance [m]

Superscripts

r	Correlation exponent (1.4) of Attou & Bolle (1997)

Subscripts

0	Flange location
1	Upstream location
2	Downstream location
3	Exit tap location
b	Bend
c	Cross-sectional
e	Effective condition for Schmidt & Friedel (1996)
$exit$	Exit
$expected$	Expected
G	Gas
I	Irreversible
L	Liquid
lo	Liquid-only
R	Reversible
sp	Single-phase
tp	Two-phase

Operators

$\langle\ \rangle$	Area-averaged quantity
$\sum$	Summation

make the specific design inefficient or impractical. Consequently, optimal heat-exchanger design requires an understanding of all possible pressure loss mechanisms.

Polymer-electrolyte membrane (PEM) fuel cells represent another example. The gas-supply channels serve to supply the PEM fuel cell with reactants and to remove excess water produced by the hydrogen-oxygen reaction. Similar to micro-heat exchangers, PEM fuel cells consist of several parallel channels in various configurations [29], which terminate at a manifold. A minor pressure loss will occur as a result. Additionally, the geometric change from a small channel to a large channel can result in the local accumulation of water [30–32]. Water accumulation will influence the distribution of reactants and minor pressure losses will influence the scale of pumps necessary to supply the reactants. As designers continue to seek improved PEM fuel cell performance [33], understanding different loss mechanisms can aid in achieving this goal.

However, understanding two-phase flow itself introduces enough complexity that researchers focus on characterizing the two-phase flow independent of any exit influences. For example, English & Kandlikar [11] designed the exit of the microchannel specifically to mitigate its influence on the results and Grimm et al. [34] used rolled up paper at the exit to prevent water accumulation near the channel exit. At times, however, experimental measurements require placing

pressure taps in the inlet/exit manifolds. Accurate determination and assessment of two-phase frictional pressure drop models requires correcting the data to isolate the two-phase frictional pressure loss component [18,35,36]. Therefore, even to investigate two-phase flow in general requires an understanding of how the minor losses influence the result.

This work investigates the pressure loss associated with a 3.23 mm wide by 0.304 mm high rectangular channel exiting into a 1.4 cm diameter circular manifold orientated 90° to the flow. The typical method to predict the pressure loss caused by exit effects relies on treating the exit as a sudden expansion and utilizing sudden expansion relations. Section 1.1 introduces the selected two-phase sudden expansion relations used in this work. Beyond Abdelall et al. [37], literature contains little discussion of the sudden expansion pressure loss for micro-scale channels, especially for rectangular microchannels. Beyond the sudden expansion, other losses at the exit can occur. Section 1.2 introduces empirical relations to account for the pressure loss associated with a 90° bend, which also occurs in this work. An outline of the experimental method to measure the two-phase pressure drop and the behavior of the air-water flow follows in Section 2. Section 3.1 discusses the validation of the experimental method.

To understand the influence of the exit requires not only investigating the exit but understanding the influence of the flow before the exit. Investigating the two-phase pressure drop and the flow behavior before the exit demonstrates that a pressure loss occurs across the exit (Sections 3.2, 3.3, and 3.4). Section 3.5 discusses the behavior of the exit pressure loss and its importance relative to the total frictional pressure drop. Comparing the measured pressure loss across the channel exit to the sudden expansion models in Section 3.6 reveals the loss in this experiment results from other mechanisms beyond the sudden expansion pressure loss. Extending the analysis to treat the pressure loss as solely a result of the 90° bend and as the combination of a sudden expansion-90° bend follows in Sections 3.7 and 3.8, respectively.

Sudden expansion pressure loss

Minor pressure losses rely on empirical measurements with the exception of the pressure loss due to a sudden area change. Defining a control volume (Fig. 1) across an area expansion and applying the conservation of mass and momentum, the relations [38]:

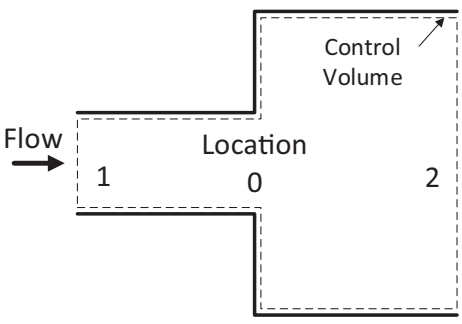

Fig. 1 – Control volume for the sudden expansion analysis.

$$\langle u_1\rangle A_1 = \langle u_2\rangle A_2 \quad \text{(Mass)} \tag{1}$$

$$\langle P_2\rangle - \langle P_1\rangle = \rho\langle u_1^2\rangle\sigma_A - \rho\langle u_2^2\rangle \quad \text{(Momentum)} \tag{2}$$

arise under the assumptions of steady, incompressible single-phase flow where no viscous losses occur in the control volume and the pressure at the flange (location 0) equals the upstream pressure (P_1). The terms u, ρ, A, and σ_A represent the axial velocity, density, cross-sectional area, and area ratio ($\sigma_A = A_1/A_2$), respectively. Subscript 1 refers to the upstream location and subscript 2 the downstream location. To combine Eqs. (1) and (2) requires relating $\langle u\rangle^2$ to $\langle u^2\rangle$ where:

$$\langle u\rangle = \frac{1}{A}\int_A u dA \tag{3}$$

defines an area-averaged axial component of velocity. For turbulent flows $\langle u^2\rangle/\langle u\rangle^2 \approx 1$. Combining Eqs. (1) and (2) gives the general relation for single-phase flow as:

$$P_2 - P_1 = \frac{\sigma_A(1-\sigma_A)}{\rho}\dot{m}^2 \tag{4}$$

where $\dot{m} = \rho\langle u_1\rangle$ and the representation of the area averaging of the pressure has been dropped for simplicity.

The mechanical energy equation defined as:

$$\int\frac{1}{2}\rho u^2\mathbf{u}\cdot\mathbf{n}dA = -\int P\mathbf{u}\cdot\mathbf{n}dA \tag{5}$$

provides a second approach to relate the pressure change across the exit to the area ratio. The vectors $\mathbf{u}$ and $\mathbf{n}$ represent the velocity vector and the unit normal to the area of the control volume, respectively. Under the same assumptions as Eqs. (1) and (2) while also neglecting body forces, Eq. (5) gives:

$$\frac{1}{2}\rho\langle u_2^3\rangle A_2 - \frac{1}{2}\rho\langle u_1^3\rangle A_1 + \langle P_2 u_2\rangle A_2 - \langle P_1 u_1\rangle A_1 = 0. \tag{6}$$

For turbulent flow $\langle u^3\rangle/\langle u\rangle^3 \approx 1$, allowing for the combination of Eqs. (1) and (5) to give:

$$P_2 - P_1 = \frac{(1-\sigma_A^2)}{2\rho}\dot{m}^2 \tag{7}$$

As $\sigma_A(1-\sigma_A) < (1-\sigma_A^2)$ for $0 < \sigma_A < 1$, Eq. (4) will predict a lower pressure change than Eq. (7). Experimental measurements agree with Eq. (4), while Eq. (7) represents the possible reversible pressure change [38].

The simplest extension of the single-phase relations to two-phase flow follow the standard homogeneous model approach of defining an equivalent single-phase flow of weighted properties such that Eq. (4) becomes:

$$\Delta P = \frac{\sigma_A(1-\sigma_A)}{\rho_{tp}}G^2 \tag{8}$$

where $\Delta P = P_2 - P_1$ and ρ_{tp} equals the two-phase density defined as:

$$\rho_{tp} = \left(\frac{\chi}{\rho_G} + \frac{1-\chi}{\rho_L}\right)^{-1} \tag{9}$$

The subscript tp stands for two-phase. The gas quality, χ, equals:

$$\chi = \frac{\rho_G Q_G}{\rho_G Q_G + \rho_L Q_L} \tag{10}$$

with G, the total mass flux, defined as:

$$G = \frac{\rho_G Q_G + \rho_L Q_L}{A_c} \tag{11}$$

Eq. (8) uses χ and G determined by the conditions in the smaller channel (location 1). Q and A_C stand for the volumetric flow rate and cross-sectional area, respectively, determined in the smaller channel. The subscripts G and L stand for the gas and liquid phase, respectively. Similarly, Eq. (7) becomes:

$$\Delta P = \frac{(1-\sigma_A^2)}{2\rho_{tp}}\dot{m}^2 \tag{12}$$

Following a similar analysis as used to define Eqs. (1) and (2), Romie [39] arrived at the two phase relation:

$$\Delta P = \frac{\sigma_A G^2}{\rho_L}\left[\chi^2\frac{\rho_L}{\rho_G}\left(\frac{1}{\alpha_1}-\frac{\sigma_A}{\alpha_2}\right)+(1-\chi)^2\left(\frac{1}{1-\alpha_1}-\frac{\sigma_A}{1-\alpha_2}\right)\right] \tag{13}$$

where α, the void fraction, equals the area occupied by the gas divided by the total cross-sectional area of the channel. Romie allowed the upstream void fraction (α_1) to vary from the downstream (α_2).

Lottes [40] simplified the analysis by neglecting the gas phase ($\chi \ll 1$) such that the pressure loss only occurs in the liquid phase and arrived at:

$$\Delta P = \frac{\sigma_A(1-\sigma_A)G^2}{\rho_L(1-\alpha)^2} \tag{14}$$

where the void fraction remains constant across the sudden expansion.

Collier & Thome [41] followed a similar analysis used to determine Eqs. (1) and (6), taking into account two phases to determine:

$$\Delta P = \frac{\rho_{tp}(1-\sigma_A^2)G^2}{2}\left[\frac{(1-\chi)^3}{(1-\alpha)^2\rho_L^2}+\frac{\chi^3}{\alpha^3\rho_G^2}\right] \tag{15}$$

Richardson [42] simplified Eq. (15) by considering only the liquid velocity such that:

$$\Delta P = \frac{(1-\sigma_A^2)\sigma_A G^2}{2\rho_L}\left[\frac{(1-\chi)^2}{1-\alpha}\right] \tag{16}$$

While the previously discussed models result from a generalization of the flow, other authors have applied the analysis to specific flows. Attou & Bolle [43] treated the sudden expansion as a conical jet originating from a small circular cross-section. Applying a momentum balance, the authors arrive at:

$$\Delta P = \sigma_A(1-\sigma_A)\vartheta^r \Upsilon G^2 + (1-\vartheta^r)\sigma_A(1-\sigma_A)\frac{G^2}{\rho_L} \tag{17}$$

$$\vartheta = \frac{3}{1+\sqrt{\sigma_A}+\sigma_A} \tag{18}$$

$$\Upsilon = \frac{\chi^2}{\alpha\rho_G}+\frac{(1-\chi)^2}{(1-\alpha)\rho_L} \tag{19}$$

Comparing the model to experimental data using the void fraction relation of Rouhani [44], the authors found $r = 1.4$ for air-water flows at small gas quality.

By restricting the flow to an annular-mist flow, Schmidt & Friedel [45] arrived at:

$$\Delta P = \frac{G^2\left[\frac{\sigma_A}{\rho_e}-\frac{\sigma_A^2}{\rho_e}-f_e\rho_e\left(\frac{\chi}{\rho_G\alpha_e}-\frac{(1-\chi)}{\rho_L(1-\alpha_e)}\right)\left(1-\sqrt{\sigma_A}\right)^2\right]}{1-\Gamma_e(1-\sigma_A)} \tag{20}$$

that depends on the relations:

$$\frac{1}{\rho_e} = \frac{\chi^2}{\rho_G\alpha_e}+\frac{(1-\chi)^2}{\rho_L(1-\alpha_e)}+\frac{\rho_L\alpha_E(1-\alpha_e)}{1-\alpha_E}\left[\frac{\chi}{\rho_G\alpha_e}-\frac{1-\chi}{\rho_L(1-\alpha_e)}\right]^2 \tag{21}$$

$$\alpha_e = 1-\frac{2(1-\chi)^2}{1-2\chi+\sqrt{1+4\chi(1-\chi)\left(\frac{\rho_L}{\rho_G}-1\right)}} \tag{22}$$

$$\alpha_E = \frac{1}{S_e}\left[1-\frac{1-\chi}{1-\chi(1-0.05We_e^{0.27}Re_e^{0.05})}\right] \tag{23}$$

$$S_e = \frac{\chi(1-\alpha_e)\rho_L}{(1-\chi)\alpha_e\rho_G} \tag{24}$$

$$We_e = G^2\chi^2\frac{d}{\rho_G\sigma}\frac{\rho_L-\rho_G}{\rho_G} \tag{25}$$

$$Re_e = \frac{G(1-\chi)d}{\mu_L} \tag{26}$$

$$\Gamma_e = 1-\sigma_A^{0.25} \tag{27}$$

$$f_e = 4.9\times10^{-3}\chi^2(1-\chi)^2\left(\frac{\mu_L}{\mu_G}\right)^{0.7} \tag{28}$$

where σ, d, and μ_L stand for surface tension, smaller pipe diameter, and liquid dynamic viscosity, respectively. The relation also depends on the effective Reynolds number (Re_e), the effective Weber number (We_e), and the effective slip ratio (S_e). Comparing data for $0<\chi<100\%$ at mass fluxes of $50-16000\ kg/m^2\cdot s$ for multiple fluid pairs showed a scatter of 61% about the prediction.

On the other hand, several authors proposed correlations not directly derived from the conservation equations. Chisholm & Sutherland [46] applied the separated flow model approach of Lockhart & Martinelli [7] and Chisholm [8] to the two-phase sudden expansion problem, such that the two-phase pressure across the sudden expansion equals its single-phase equivalent multiplied by a scaling factor. The relation thus equals:

$$\Delta P = \frac{G^2}{\rho_L}\sigma_A(1-\sigma_A)(1-\chi)^2\left[1+\frac{C_h}{X_h}+\frac{1}{X_h^2}\right] \tag{29}$$

$$X_h = \left(\frac{\rho_g}{\rho_L}\right)^{0.5}\frac{(1-\chi)}{\chi} \tag{30}$$

$$C_h = \left\{1+0.5\left[1-\left(\frac{\rho_G}{\rho_L}\right)\right]^{0.5}\right\}\left\{\left(\frac{\rho_G}{\rho_L}\right)^{0.5}+\left(\frac{\rho_L}{\rho_G}\right)^{0.5}\right\} \tag{31}$$

which applies only for turbulent flow in rough tubes.

Wadle [47] considered the pressure loss as being proportional to the difference in the dynamic pressure head such that:

$$\Delta P = \left(1-\sigma_A^2\right)\frac{\dot{m}^2}{2}K^*\left[\frac{\chi^2}{\rho_G}+\frac{(1-\chi)^2}{\rho_L}\right] \tag{32}$$

For experimental data at $0<\chi<7\%$ in an area expansion of a 16 mm diameter tube into a 80 mm diameter tube with mass fluxes of 4500–11000 kg/m^2·s, the authors found K^* equals 0.83 for air-water flows.

The equations for a sudden area expansion presented above apply to conventional scale channels. In the case of micro-scale tubes/channels, Abdelall et al. [37] investigated the pressure loss for air-water flow through a 0.16 mm diameter tube into a 0.84 mm diameter tube. The authors used the relations:

$$\Delta P = \Delta P_R + \Delta P_I \tag{33}$$

$$\Delta P_R = \frac{G^2}{2}\left(\frac{1-\sigma^2}{(\rho'')^2}\right) \tag{34}$$

$$\Delta P_I = \frac{G^2}{2\rho_L}\left[\frac{2\rho_L}{\rho'}\sigma_A(\sigma_A-1)-\rho_{tp}\frac{\rho_L}{(\rho'')^2}(\sigma_A-1)\right] \tag{35}$$

where Eq. (34) accounts for reversible pressure loss while Eq. (35) accounts for irreversible pressure losses. Eqs. (34) and (35) depend on:

$$\rho' = \left[\frac{(1-\chi^2)}{\rho_L(1-\alpha)}+\frac{\chi^2}{\rho_G\alpha}\right]^{-1} \tag{36}$$

$$\rho'' = \left[\frac{(1-\chi)^3}{\rho_L^2(1-\alpha)^2}+\frac{\chi^3}{\rho_G^2\alpha^2}\right]^{-0.5} \tag{37}$$

When using the homogeneous void fraction (β) defined as:

$$\beta = \frac{Q_G}{Q_G+Q_L} \tag{38}$$

Eq. (33) overestimated the data. However, using the ideal annular flow slip ratio of $S=(\rho_L/\rho_G)^{1/3}$ to define the void fraction as:

$$\alpha = \frac{Q_G}{Q_G+SQ_L} \tag{39}$$

in Eq. (33), the prediction agreed with the experimental data for liquid-only Reynolds numbers (Re_{lo}) between 2500 and 3530.

With the exception of the models of Chisholm & Sutherland (Eq. (29)), Wadle (Eq. (32)), and the homogeneous model, the sudden expansion models rely on a correlation for the void fraction, which acts as a closure model for the sudden expansion relations. However, several correlations exist. In addition to Eqs. (38) and (39), Rouhani [44] proposed:

$$\alpha = \frac{\frac{\chi}{\rho_G}}{\frac{1+0.12(1-\chi)}{\rho_{tp}}+\frac{W_{rel}}{\dot{m}}} \tag{40}$$

$$W_{rel} = \frac{1.18}{\sqrt{\rho_L}}\left[g\sigma(\rho_L-\rho_G)\right]^{0.25} \tag{41}$$

where g equals the acceleration due to gravity. Both Wadle and Attou & Bolle used Eq. (40) when comparing to experimental data. In evaluating the sudden expansion models for air-water flow in a rectangular duct of dimensions 3 mm by 6 mm expanding into a rectangular duct of 3 mm by 9 mm, Chen et al. [48] used the relation defined by Kawahara et al. [49] as:

$$\alpha = \frac{0.03\beta^{0.5}}{1-0.97\beta^{0.5}} \tag{42}$$

The authors found that the model of Wadle predicted the experimental data with a mean deviation of 200% at gas qualities between 0.001 and 0.8 with mass fluxes between 100 and 700 kg/m^2·s.

Pressure loss in a 90 degree bend

The sudden expansion in this work also includes the flow passing through a 90° bend. Unlike the sudden expansion models, determining the pressure loss resulting from a 90° bend requires purely empirical relations. In single-phase flows, a loss occurring at a bend follows the relation:

$$\Delta P_b = \kappa_b\frac{G^2}{2\rho} \tag{43}$$

where the subscript b stands for bend. The resistance coefficient (κ) accounts for the geometry of the bend where experimental measurements determine its value. Predicting the two-phase pressure loss in a bend typically follows the work of Lockhart & Martinelli [7] in which the two-phase loss in a bend equals a scaling factor (ϕ_b^2) multiplying the single-phase loss (Eq. (43)).

Chishom [50] determined $\phi_{b,L}^2$ as:

$$\phi_{b,L}^2 = 1+\left(\frac{\rho_L}{\rho_G}-1\right)\left\{B\chi(1-\chi)+\chi^2\right\} \tag{44}$$

where the term B approximates the change in the momentum flux resulting from a change in velocity ratio between phases and equals:

$$B = 1+\frac{2.2}{\kappa\left(2+\frac{R}{D}\right)} \tag{45}$$

for a 90° bend. The term R/D stands from the radius of the bend divided by the diameter of the channel. Calculating the two-phase pressure loss from a bend ($\Delta P_{b,tp}$) from Eq. (44) requires multiplying Eq. (44) by Eq. (43) using the liquid density. Chisholm arrived Eq. (44) under the assumptions of horizontal, incompressible, non-evaporating flow approximated as a homogenous flow with constant changes in the velocity ratio.

Paliwoda [51] sought to provide a generalized loss equation for conventionally sized pipe system components. In a 90° bend containing turbulent flow of refrigerants, Paliwoda proposed:

$$\phi_{b,G}^2 = \left[\frac{\rho_G}{\rho_L}\left(\frac{\mu_L}{\mu_G}\right)^{0.25}+2.7\chi\left(1-\frac{\rho_G}{\rho_L}\left(\frac{\mu_L}{\mu_G}\right)^{0.25}\right)\right][1-\chi]^{0.333}+\chi^{2.276} \tag{46}$$

As the two-phase flow multiplier depends on the gas conditions, the single-phase loss (Eq. (43)) uses the gas density to solve for $\Delta P_{b,tp}$.

In a private communication with Azzi et al. [52], Kuhn & Morris [53] proposed the relation:

$$\phi_{b,L}^2 = \frac{1}{(1-\chi)^2}\left[\frac{\rho_L}{\rho_{tp}}\left\{1+\chi\left(\frac{\rho_{tp}}{\rho_G}-1\right)(B-1)\right\}\right] \quad (47)$$

as a modification of the relation proposed by Chisholm.

Other authors have proposed relations based on the homogeneous flow model. Sookprasong et al. [54] proposed:

$$\Delta P_{b,tp} = \frac{\kappa}{2}[\rho_L U_L + \rho_G U_G](U_G + U_L) \quad (48)$$

where U signifies a superficial velocity. Experimental measurements in a 5.08 cm diameter pipe generally followed the prediction of Eq. (48).

Experimental method

This work follows the experimental method detailed in Lewis & Wang [55]. The experiment generates flows with liquid Reynolds numbers (Re_L) of 0.0277, 0.277, 0.55, and 5.55 with gas Reynolds numbers (Re_G) varying between 18.2 and 197 for each liquid Reynolds number in the microchannel. The combination of Reynolds numbers produce a liquid-only Reynolds number (Re_{lo}) between 0.35 and 9.19. These conditions represent typical conditions in a fuel cell. The calculation of different properties relies on standard fluid properties of humid air and water at 20°C shown in Table 1.

Experimental assembly

Fig. 2 shows the experimental set-up for the measurement of the two-phase pressure and visualization of the flow behavior. The horizontally aligned microchannel assembly (Fig. 2A) forms a 3.23 mm by 0.304 mm by 164 mm ($w \times h \times L$) rectangular microchannel. The channel consists of three materials: 6061 aluminum for the base with a contact angle (γ) of 76°±8°, 304 full hard stainless steel ($\gamma = 82° \pm 7°$) forming the sides, and polycarbonate ($\gamma = 81° \pm 7°$) forming the top. In this work, the stated uncertainties are at a 95% confidence level.

A syringe pump (New Era Pump System NE-300, Fig. 2B) supplies room temperature (20°C±2°C) deionized water to the channel through a 365 μm hole in the aluminum base located 10 mm downstream from the air inlet. Four different liquid flow rates of 177 μL/hr, 1.77 mL/h, 59.07 μL/min, and 590.7 μL/min produce superficial liquid velocities of 5.0×10^{-5}, 5.0×10^{-4}, 1.0×10^{-3}, and 1.0×10^{-2} m/s, respectively.

MKS 100B mass flow controllers inside a Scribner and Associates 850e Fuel-cell Test Station (Fig. 2C) control the air flow from the main air supply within ±20 mL/min. The air passes through a bubble humidifier containing 1500 mL of DI-water to achieve 100% relative humidity (Fig. 2D) before entering the microchannel. The gas flow rates vary from 30 to 50–325 mL/min in 25 mL/min increments producing superficial gas velocities between 0.51 and 5.50 m/s.

A 1 cm diameter hole acts as the inlet manifold while a 1.4 cm diameter hole acts as an outlet manifold. The minimum straight distance between the edge of the manifolds defines the channel length. Fig. 3a illustrates the exit geometry for this experiment. The two-phase flow expands from a rectangular duct into a circular manifold oriented 90° relative to the flow direction. The top of the channel extends over the exit manifold, while the side walls extend approximately 2 mm over the manifold, before expanding to the full width of the manifold. Therefore, the flow first sees the bottom of the channel expand before the sides expand. Using the diameter of the manifold as the expansion area gives a value of 0.0064 for the area ratio ($\sigma_A = A_1/A_2$).

Table 1 – Fluid properties.

Property	Air	Water
Density (kg/m^3)	1.19	998.3
Viscosity ($kg/m{\cdot}s$)	1.846×10^{-5}	1.002×10^{-3}
Surface tension (N/m)	72.86×10^{-3}	

Pressure measurement

A Setra 230 differential pressure transducer (Fig. 2E) with a range of ±0.5 psi (3.447 kPa) measures the difference between two pressure taps in the microchannel with an accuracy of ±0.0025 psi (17.2 Pascals). The measured pressure difference occurs between two sets of taps as shown in Fig. 3b. The first measurement measures the difference over a 154 mm length of the channel, between Tap 1 located at z = 0 mm and Tap 2 located 12 mm before the exit at z = 152 mm—where z denotes a downstream coordinate. This measurement provides the two-phase pressure drop representative of the flow dynamics. The second measurement takes the pressure difference between the entrance (Tap 1 at z = 0 mm) and a pressure tap (Tap 3) located in the exit manifold (z = 171 mm). This measurement provides a pressure drop that will include any exit effects. A valve allows switching between the two measurements (Fig. 2). The measurement between Taps 1 and 2 occurs first followed by a measurement between Taps 1 and 3.

Visualization and film thickness measurements

The clear polycarbonate sheet forming the top of the channel allows optical access for a DSLR camera (Canon Rebel T3, Fig. 2F) to capture images of the entire channel length in 5 s increments. Under the test conditions, the air and water form a stratified flow pattern. A MATLAB code processes the images to extract the location of the water-air interface, defining the water film thickness. Trapezoidal numerical integration of the water film thickness along the channel divided by the length of the film gives an equivalent film thickness—essentially the film that has the same area as the experimental data but produces a flat interface between the fluids. Eighty pixels compose the width of the channel (3.23 mm), meaning each pixel represents 0.04 mm. A Kline-McClintock uncertainty analysis gives the uncertainty of the film thickness as 0.11 mm.

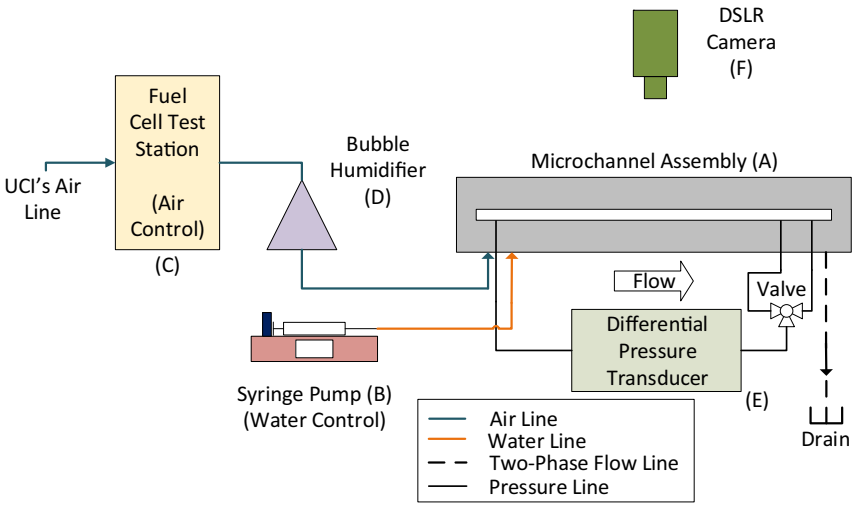

Fig. 2 – Schematic diagram of the experimental set-up.

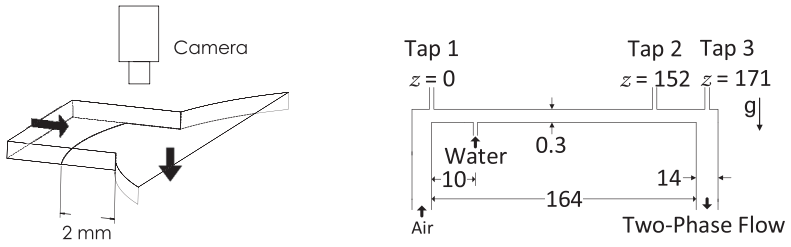

(a) Diagram of the exit geometry of the microchannel.

(b) Pressure tap locations. Dimensions are in millimeters.

Fig. 3 – Detailed diagram of the microchannel assembly.

Results and discussion

Single-phase validation

Single-phase gas flow experiments were conducted for validation of the experimental apparatus. For single phase flow, the pressure follows:

$$\left(\frac{dP}{dz}\right) = f\frac{\rho U_G^2}{2D_H} \tag{49}$$

where D_H represents the hydraulic diameter. The superficial gas velocity (U_G) equals the gas volumetric flow rate (Q_G) divided by the cross-sectional area (A_c). The Darcy friction factor (f) depends on the gas Reynolds number and equals:

$$f = \frac{\overline{C}}{Re_G} \tag{50}$$

where the correlation constant ($\overline{C}$) depends on the aspect ratio of the channel as:

$$\overline{C} = 96\left(1 - 1.35532\alpha^* + 1.9467\alpha^{*2} - 1.7012\alpha^{*3} + 0.9564\alpha^{*4} - 0.2537\alpha^{*5}\right) \tag{51}$$

given by Kakac et al. [56] from fitting the exact solutions of Shah & London [57] for different aspect ratios (α^*). The aspect ratio (α^*) equals the smallest dimension divided by the largest dimension.

Fig. 4a shows the comparison between the experimentally measured pressure drop and the theoretical value measured between Taps 1 & 2. The data fall within ±4% for all experiments except for the two lowest. At gas velocities of 0.51 m/s and 0.85 m/s, the measurements fall below the predicted value by 17% and 7%, respectively. Fig. 4b shows the comparison between the experimentally measured pressure drop and the theoretical value measured between Taps 1 & 3. The experiments fall within ±4.5% for all experiments except for the two lowest. At 0.51 m/s and 0.85 m/s, the measurements fall below the predicted value by 17% and 6%, respectively. The similarity in the deviation from theory for both measurements indicates that for single-phase flow, the exit accounts for less than 1% of the deviation. The error bars for pressure in Fig. 4 account for the ±17.2Pa accuracy of the pressure transducer. The superficial gas velocity equals the volumetric flow rate of gas divided by the cross-sectional area. Utilizing the Kline-McClintock method for the equation $U_G = Q_G/A_c$, gives a velocity uncertainty of ±0.34m/s at a gas velocity of 0.51 m/s to ±0.43m/s at 5.5 m/s.

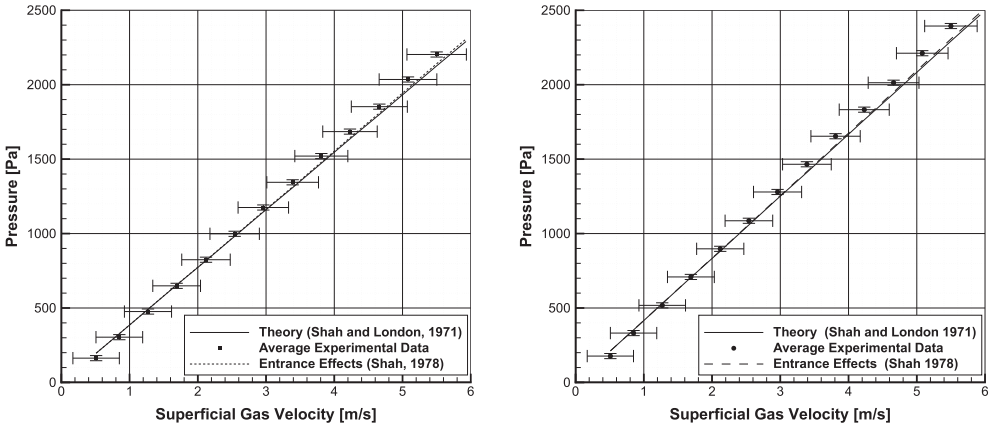

(a) Pressure Taps 1-2. (b) Pressure Taps 1-3.

Fig. 4 – Single-phase pressure drop versus superficial gas velocity.

The location of the first tap ($z = 0$) means that the pressure drop will include entrance effects. To account for the entrance effects, Shah defines an apparent Fanning friction factor [58] that replaces Eq. (50). The single-phase pressure with entrance effects results from using four times the apparent friction factor in Eq. (49). Fig. 4a and b also show a comparison of the experimental data to the predicted pressure drop with entrance effects. The entrance effects reduce the difference between the prediction and the experimental measurements by 1%; thus, the pressure tap location does not significantly influence the results.

Two-phase pressure results

The two-phase pressure results indicate a difference between measurements before the channel exit (Taps 1 & 2) versus after the exit (Taps 1 & 3). Characterizing the two-phase pressure drop relies on the gas two-phase flow multiplier (ϕ_G^2) defined as the ratio of the experimentally measured two-phase pressure to the gas single-phase pressure. Fig. 5 shows a comparison between ϕ_G^2 versus superficial gas velocity (U_G) for measurements taken between Taps 1 & 2 and between Taps 1 & 3. The experimental data points for Tap 2 represent a 30 min average of the measured two-phase pressure for the three lowest superficial liquid velocities and 5 min averages for the $U_L = 1.0 \times 10^{-2}$ m/s data set. The measurements shown for Tap 3 represent the average of all the experimental data points for a given superficial gas velocity. Both measurements show the same trend of ϕ_G^2 decreasing with increasing superficial gas velocity and ϕ_G^2 increasing with increasing superficial liquid velocity. However, the two measurements differ in terms of the magnitude of ϕ_G^2. The measurement between Taps 1 & 3 fall significantly higher than the corresponding measurements between Taps 1 & 2.

The data for Taps 1 & 3 in Fig. 5 only represent the average measurement of ϕ_G^2 for clarity. Looking at the individual experimental data points for ϕ_G^2 reveals an interesting behavior (Fig. 6). Particularly at the lower superficial gas velocities, the value of ϕ_G^2 varies well outside the uncertainty of the measurement determined from the Kline-McClintock method for the equation $\phi_G^2 = P_{tp}/P_G$. Consequently, some physical mechanism—such as a change in flow behavior—must cause the difference between individual measurements and the difference between the two test cases (Taps 1–2 and Taps 1–3).

Flow behavior along the channel

With the test conditions remaining the same, a change in the flow behavior likely results in the difference between individual measurements for Taps 1 & 3. In the channel, the air-water flow forms as a stratified flow, in which a water film moves along a side wall, filling the entire height of the channel but not the entire channel width. Visualization of the water film showed the film did not change during the duration of an experiment in the region between Taps 1 and 2. The pressure signals indicate a steady condition in the channel as well. Fig. 7 shows 1 minute of a 10 minute sample of the pressure time trace for $U_G = 5.08$ m/s at $U_L = 1.0 \times 10^{-2}$ m/s. The signal remains steady about the mean, a characteristic shared by all of the experiments. Therefore, after the development of the stratified flow, the mean pressure signal remains unchanged throughout the experiment.

The pressure signal, however, does not remain a constant value; Fig. 7 shows both short and long period oscillations. Fast-Fourier transforms (FFT) of the single-phase and of the two-phase pressure signals indicate that the relatively high frequency oscillation results from the bubble humidifier based on the frequency of bubble formation. The humidifier introduces a primary frequency of 2 Hz at $U_G = 0.51$m/s to 10 Hz at $U_G = 5.50$m/s. The longer period oscillation results from the mechanical oscillation from the syringe pump. Zeng et al. [59] showed that pressure oscillations seen in experiments correspond to the mechanical frequency of the syringe pump (f_m). The relation for f_m proposed by Zeng et al. [59], gives a period of oscillation equal to 17.5 s. Based on a power-spectral density calculation, the long wavelength in Fig. 7 has a period of 21 s. Therefore, the prediction differs by 3.5 s but does indicate that the oscillation results from the syringe pump.

The steady dynamics allowed for the measurement of the two-phase pressure between Taps 1 & 2 first before

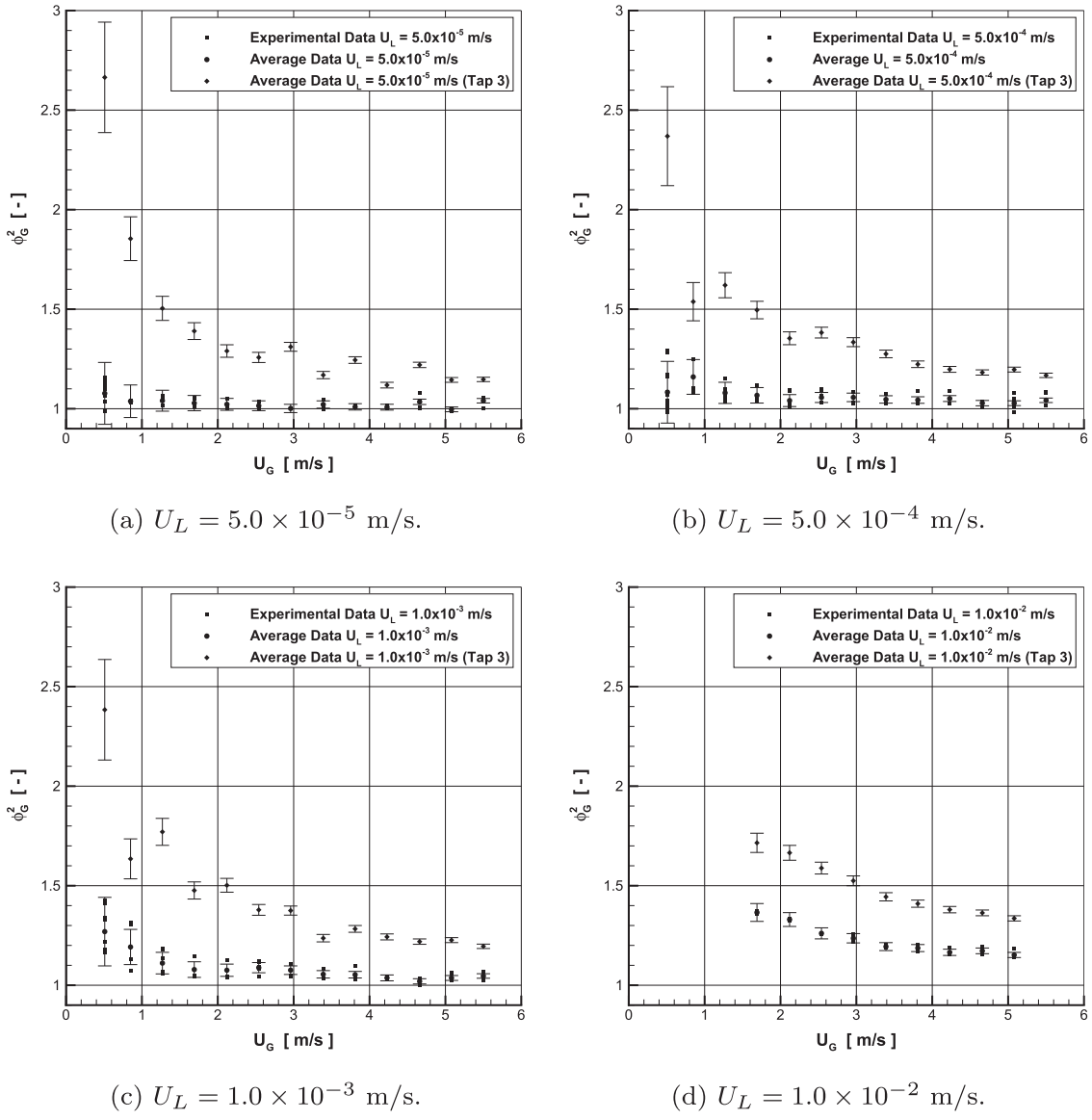

(a) $U_L = 5.0 \times 10^{-5}$ m/s. (b) $U_L = 5.0 \times 10^{-4}$ m/s.

(c) $U_L = 1.0 \times 10^{-3}$ m/s. (d) $U_L = 1.0 \times 10^{-2}$ m/s.

Fig. 5 – Experimental gas two-phase flow multiplier versus superficial gas velocity comparing data at Tap 2 and Tap 3.

subsequently measuring the two-phase pressure between Taps 1 & 3 by switching the valve. While ideally the measurements would occur simultaneously, the steady dynamics of the system allowed for the sequential measurements.

While the water film did not change during an experiment, the water film did change between different experiments conducted at the same test conditions. Fig. 8 shows a comparison between water films across several test conditions. The compressed aspect ratio of Fig. 8 causes the wavy appearance of the films. Typically, the water film changes the most around the water inlet. For example, Test 2 showed a water droplet near the water inlet separate from the water film whereas Test 1 had a smooth connection to the inlet for $U_G = 4.23$ m/s at $U_L = 1.0 \times 10^{-2}$ m/s (Fig. 8b). The films, however, do remain similar. As the measurements between Taps 1 & 2 did not show such extreme variation outside of the uncertainty (Fig. 5) when compared to the variation of measurements between Taps 1 & 3 (Fig. 6), the change in the film behavior between experiments can neither account for the variation nor the differences between the two test cases (Taps 1–2 and Taps 1–3).

Isolating the influence of the expansion to the exit manifold

With the behavior of the stratified flow before the exit unable to account for the variations of the measurements, determining whether the two-phase pressure measurements between Taps 1 & 2 or between Taps 1 & 3 better represent the pressure loss associated with stratified flow will narrow the focus to the water accumulation at the channel exit. In a stratified flow, a distinct boundary exists between the air and the water. Neglecting the capillary forces would mean each phase experiences the same streamwise pressure drop. To first approximation, one could assume that the velocity at the interface between the fluids equals zero—i.e. a separating wall. To calculate the two-phase pressure drop would then

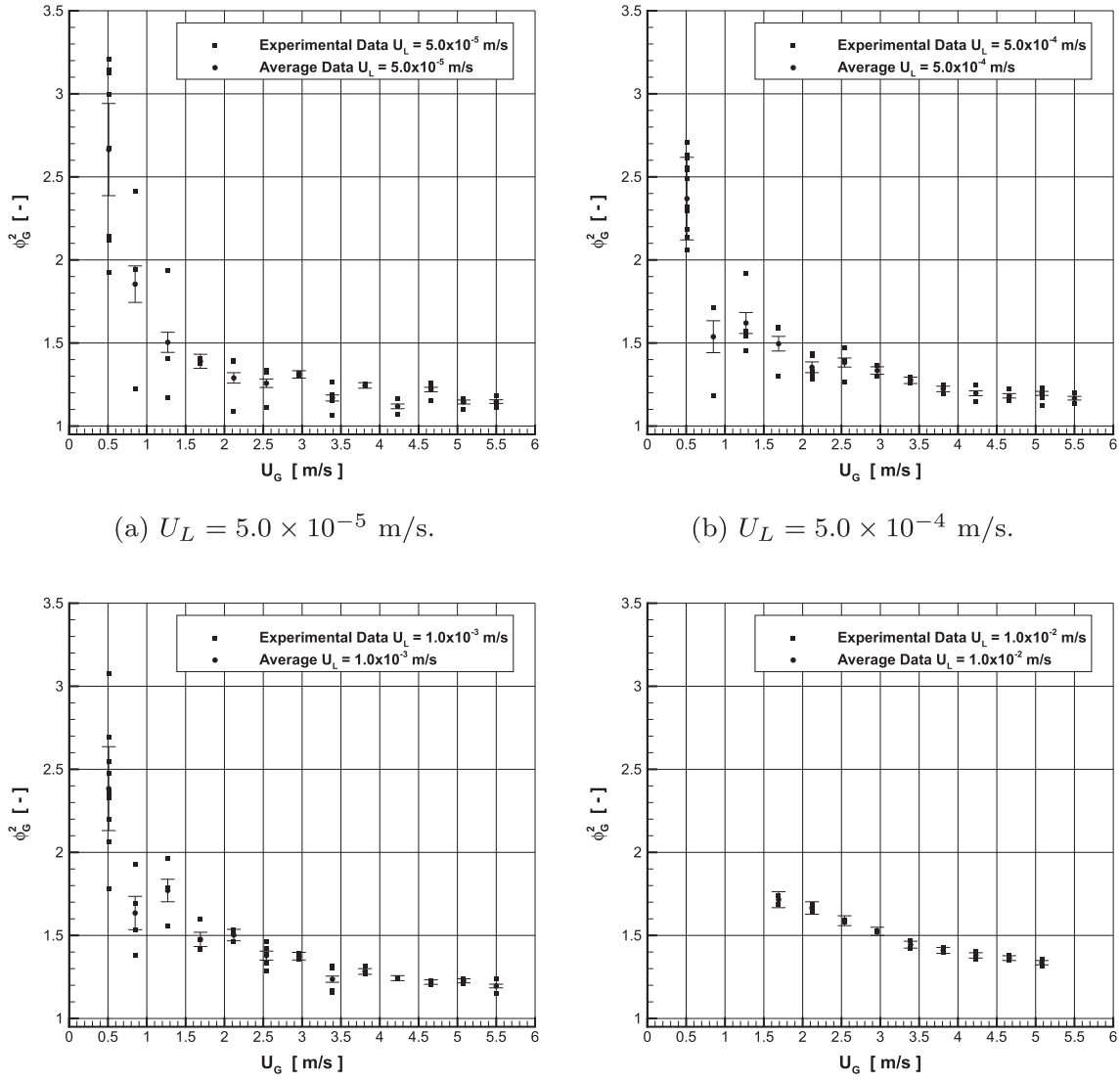

(a) $U_L = 5.0 \times 10^{-5}$ m/s. (b) $U_L = 5.0 \times 10^{-4}$ m/s.

(c) $U_L = 1.0 \times 10^{-3}$ m/s. (d) $U_L = 1.0 \times 10^{-2}$ m/s.

Fig. 6 – Experimental gas two-phase flow multiplier versus superficial gas velocity measured between Taps 1 & 3.

only require calculating the single-phase pressure drop in a channel of reduced width. Visualization of the water film allowed for the determination of the water film thickness. By subtracting the water film thickness from the channel width gives a single-phase gas flow in a smaller channel. Eqs. (49)–(51) determine the pressure drop of the channel of reduced width.

Fig. 9 compares the reduced width calculation to the two-phase measurement between Taps 1 & 2. The reduced width method shows that the two-phase pressure measurements between Taps 1 & 2 well represent the stratified flow behavior. The error bars for the pressure measurement account for the ±17.2Pa accuracy of the pressure transducer. The error bars for the reduced width calculation represent the uncertainty in the film thickness of ±0.11mm. Even with the uncertainty in the measurement, the water film does not block off enough of the channel width to produce the pressure drop seen in the measurement between Taps 1 & 3. Therefore, a loss must occur at the exit of the channel as the flow behavior agrees with the two-phase pressure measurement between Taps 1 & 2.

Investigating the water accumulation at the channel exit gives insight into the variation of the measured pressure between Taps 1 & 3 for a given test condition. The flow behaved two ways at the exit: periodic oscillations or stationary. In the periodic case, water at the exit could periodically block the channel (Fig. 10a and b) and then break apart (Fig. 10c and d). Under the same test conditions, the water film would thicken near the channel/manifold edge (Fig. 11a and b) and remain stationary for the duration of the experiment. Although the water appears to block the entire channel exit, the camera resolution prevents determining how close to the far wall the water extends. Unfortunately, top down images do not provide information on how the water blocks the channel height as a function of the channel width. For the test velocities of $U_L = 5.0 \times 10^{-5}$ to 1.0×10^{-3} m/s between $U_G = 0.51$ & 1.27 m/s,

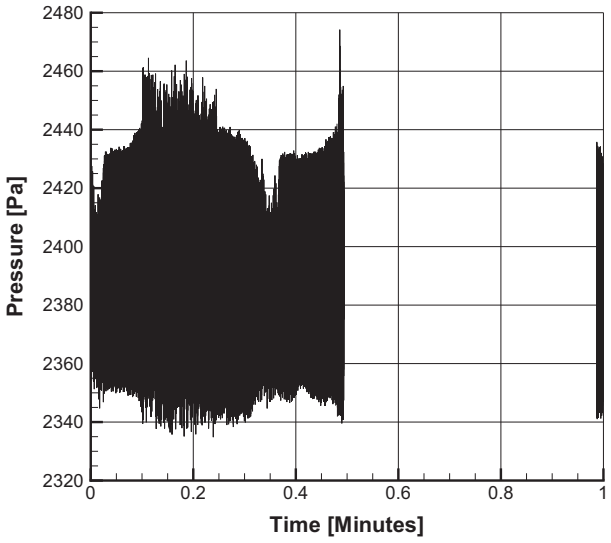

Fig. 7 – Representative pressure time trace shown for U_G = 5.08 m/s at $U_L = 1.0 \times 10^{-2}$ m/s.

the periodic case corresponds to the low ϕ_G^2 while the stationary case corresponds to the higher ϕ_G^2 in Fig. 6. In the intermediate range of the gas two-phase flow multiplier both the periodic and stationary behavior can produce similar pressure measurements. Additionally, as the gas velocity increases, it becomes difficult to discern the flow behavior at the exit and appears to approach the stationary behavior. The possibility of different behaviors at the exit could lead to flow maldistribution in parallel channels.

Pressure increase resulting as the air-water flows from the channel to the exit manifold

As discussed in Sections 3.2, 3.3, and 3.4, the behavior of the flow in the channel cannot account for the differences between the measurements of Taps 2 and 3. Therefore, the pressure difference results from a loss associated with the geometry change from the channel to the manifold. Fig. 12 shows the pressure change across the channel exit (ΔP_{exit}) defined as:

$$\Delta P_{exit} = P_{1,3} - P_{expected} \tag{52}$$

where $P_{1,3}$ equals the experimentally measured pressure drop between Taps 1 & 3 and the expected pressure with no loss ($P_{expected}$) equals:

$$P_{expected} = \phi_G^2 P_{sp,3} \tag{53}$$

where $P_{sp,3}$ equals the single-phase pressure measurement between Taps 1 & 3 while ϕ_G^2 equals the gas-two phase flow multiplier determined from the two-phase pressure

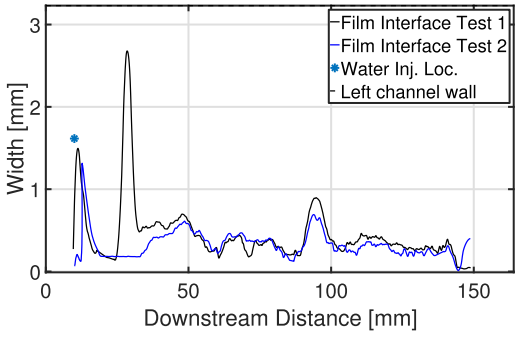

(a) $U_G = 0.85$ m/s and $U_L = 5.0 \times 10^{-4}$ m/s.

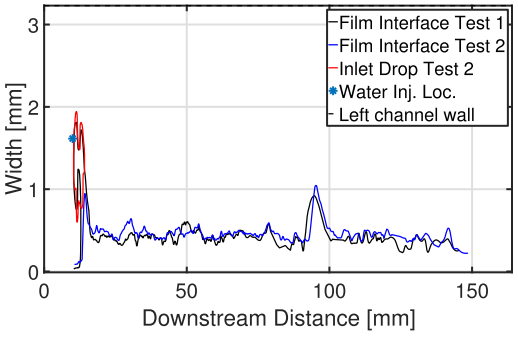

(b) $U_G = 4.23$ m/s and $U_L = 1.0 \times 10^{-2}$ m/s.

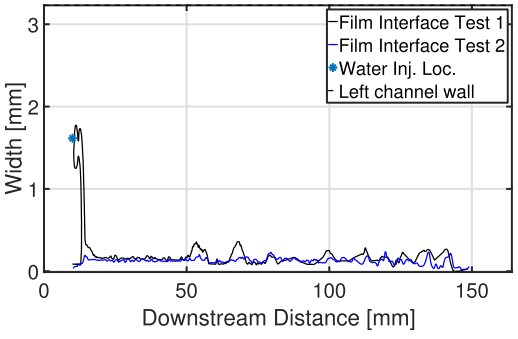

(c) $U_G = 5.08$ m/s and $U_L = 1.0 \times 10^{-3}$ m/s.

Fig. 8 – Comparison of the film thickness for different experiments (Color).

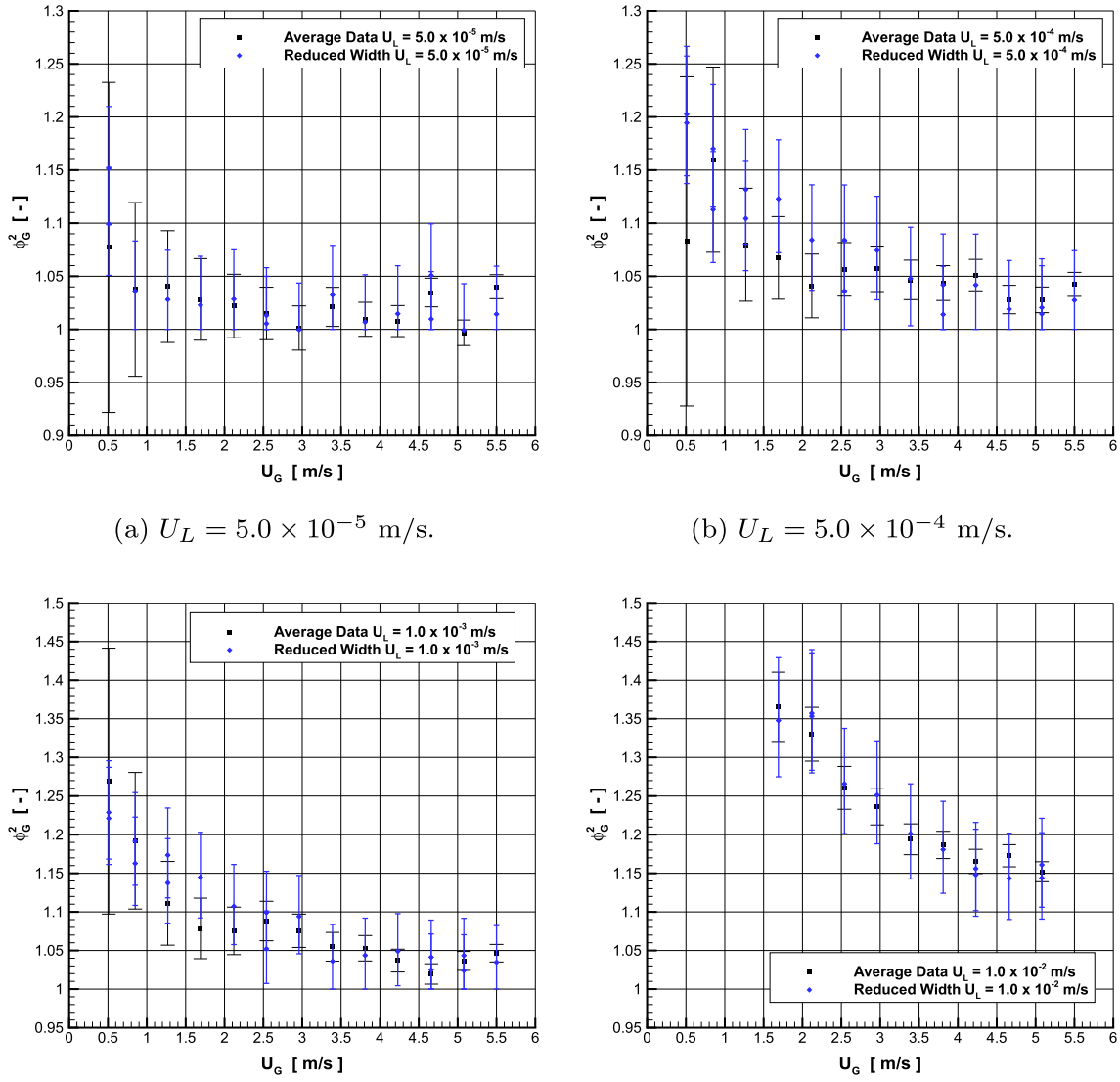

(a) $U_L = 5.0 \times 10^{-5}$ m/s. (b) $U_L = 5.0 \times 10^{-4}$ m/s.

(c) $U_L = 1.0 \times 10^{-3}$ m/s. (d) $U_L = 1.0 \times 10^{-2}$ m/s.

Fig. 9 – Comparison of the gas two-phase flow multiplier versus superficial gas velocity determined by experimental measurement and the reduced width method between Taps 1 & 2.

measurements between Taps 1 & 2. Defining ΔP_{exit} in this manner removes the contribution of the frictional two-phase pressure drop, isolating the pressure increase due to the geometry change at the channel exit.

Interestingly, the data does not show a clear dependence on the superficial liquid velocity (Fig. 12). Additionally, the exit pressure data for $U_L = 1.0 \times 10^{-3}$ and 1.0×10^{-2} m/s show a clear dependence on the superficial gas velocity, showing an increase with increasing U_G but appearing to reach a 400 Pa plateau after $U_G = 3.0$ m/s. This indicates that if a channel has sufficient length, the relatively high frictional pressure will mask the influence of the exit. While this could aide in experimental design when looking to correlate the two-phase pressure, ideally models would predict the magnitude of exit losses.

Based on the behavior of the pressure loss across the exit, set parameters determine the magnitude of the exit pressure loss. For this experiment, the exit geometry and the surface tension remain constant. With only a single fluid pair (air-water), a comment cannot be made on the influence of surface tension, and will instead focus on the geometric effects—particularly focusing on treating the exit as a sudden expansion and accounting for the 90° bend.

Comparison of sudden expansion models to the experimental data

As shown in Fig. 3a, the microchannel ends at a circular manifold located 90° relative to the flow path, which equates to a sudden expansion. Subsection 1.1 introduced several

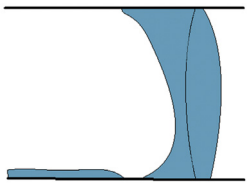

(a) Schematic: relative time = 0 seconds.

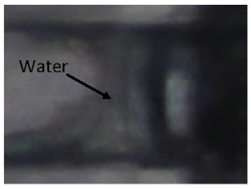

(b) Image: relative time = 0 seconds.

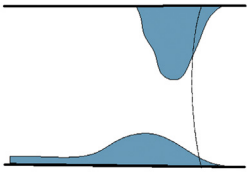

(c) Schematic: relative time = 5 seconds.

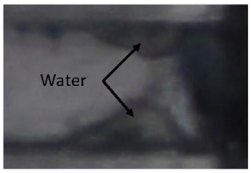

(d) Image relative time = 5 seconds.

Fig. 10 – Observed periodic behavior of the water at the channel exit viewed top-down (flow left to right; water indicated as blue). (For interpretation of the references to color in this figure legend, the reader is referred to the Web version of this article).

models for the pressure change resulting from a sudden expansion. Of the selected models, the model of Abdelall et al. [37] came closest to the experimental data (Fig. 13) with a mean absolute percent error of 96%. The mean absolute percent error ($|\bar{e}_{\%}|$) equals:

$$|\bar{e}_{\%}| = \frac{1}{n}\sum_{i=1}^{n}|\delta^{*}P_i| \tag{54}$$

where n equals the number of data points and $\delta^{*}P_i$ equals the two-phase pressure drop predicted minus the experimental two-phase pressure drop, both divided by the experimental measurement. The other selected correlations predicted pressures less than those of Abdelall et al., deviating further from the experimental results. The relation of Lottes, defined by Eq. (14), stands as an outlier. Eq. (14) holds for $\chi \ll 1$ such that the void fraction also becomes small. In this case, the gas phase dominates, making the term $(1-\alpha)$ small, resulting in unrealistic pressures using Eq. (14) for the lowest superficial liquid velocity data set. Thus, the following discussion of the sudden expansion relations excludes the relation of Lottes.

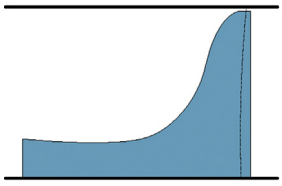

(a) Schematic.

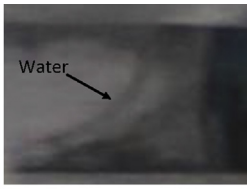

(b) Image.

Fig. 11 – Observed stationary behavior of the water at the channel exit viewed top-down (flow left to right; water indicated as blue). (For interpretation of the references to color in this figure legend, the reader is referred to the Web version of this article).

Several possible explanations could account for the difference between the experimental data and the prediction of the models. All of the selected models assume a turbulent flow in a circular pipe. The difference between a laminar or turbulent flow for a sudden expansion comes from the treatment of the area averaged velocity terms. For single-phase turbulent flow $\langle w^2\rangle/\langle w\rangle^2 \approx 1$, allowing for the direct substitution of the continuity equation into the conservation of momentum equation. Numerically integrating the analytical solution for the single-phase velocity profile in a rectangular duct for both $\langle w^2\rangle$ and $\langle w\rangle^2$ showed that $\langle w^2\rangle/\langle w\rangle^2 \approx 1.2$. Therefore a correction of 20% to the turbulent prediction will account for laminar flow in a rectangular duct. However, a 20% increase of the prediction will not account for the difference between the measurement and the prediction. Abdelall et al. also took into account the reversible pressure change derived from the energy equation that would scale 2 to 1 for laminar to turbulent flow, which also cannot increase the prediction to the experimental measurement. Therefore, neither the flow type nor the geometry can account for the difference.

This leaves the correlations for the void fraction (α) as a possible reason for the deviation between the measured pressure loss and the predictions. As detailed in subsection 1.1, several void fraction correlations exist. For this experiment, the flow formed a stratified pattern which allows for the determination of the void fraction in the channel as:

$$\alpha = 1 - s_L \tag{55}$$

where s_L equals the liquid saturation defined as the ratio of the volume of liquid to the volume of the channel. For stratified flow, this equals the ratio of the water film thickness to the width of the channel. However, using Eq. (55) in the sudden expansion model defined by Eq. (33) changed the exit pressure by only 0.1–20 Pa. Thus, the void fraction does not account for the difference between the prediction and the measurement.

Finally, the scale of the experiments could explain the difference between the predictions and the experimental results. Of the selected models, only Abdelall et al. [37] tested geometries with a hydraulic diameter less than 1 mm. As a consequence, the models neglect any influence of surface tension which becomes dominant at small scales. Abdelall et al. also did not need to take into account surface tension because the test liquid Reynolds numbers fall in the range where surface tension forces become small. While accounting for the surface tension would add an additional term to the momentum equation, the single fluid pair in this experiment precludes the possibility of analyzing its influence on the sudden expansion relations.

Based on the comparison of existing models of the sudden expansion to the measured pressure loss occurring across the exit of the microchannel, the experiment does not compare well to the sudden expansion models. However, the comparison itself breaks down. Sudden expansion correlations assume the flow remains horizontal and has achieved fully-developed flow at both locations used to determine the pressure difference. As Fig. 3 shows these assumptions break down. The flow likely has not become fully developed before

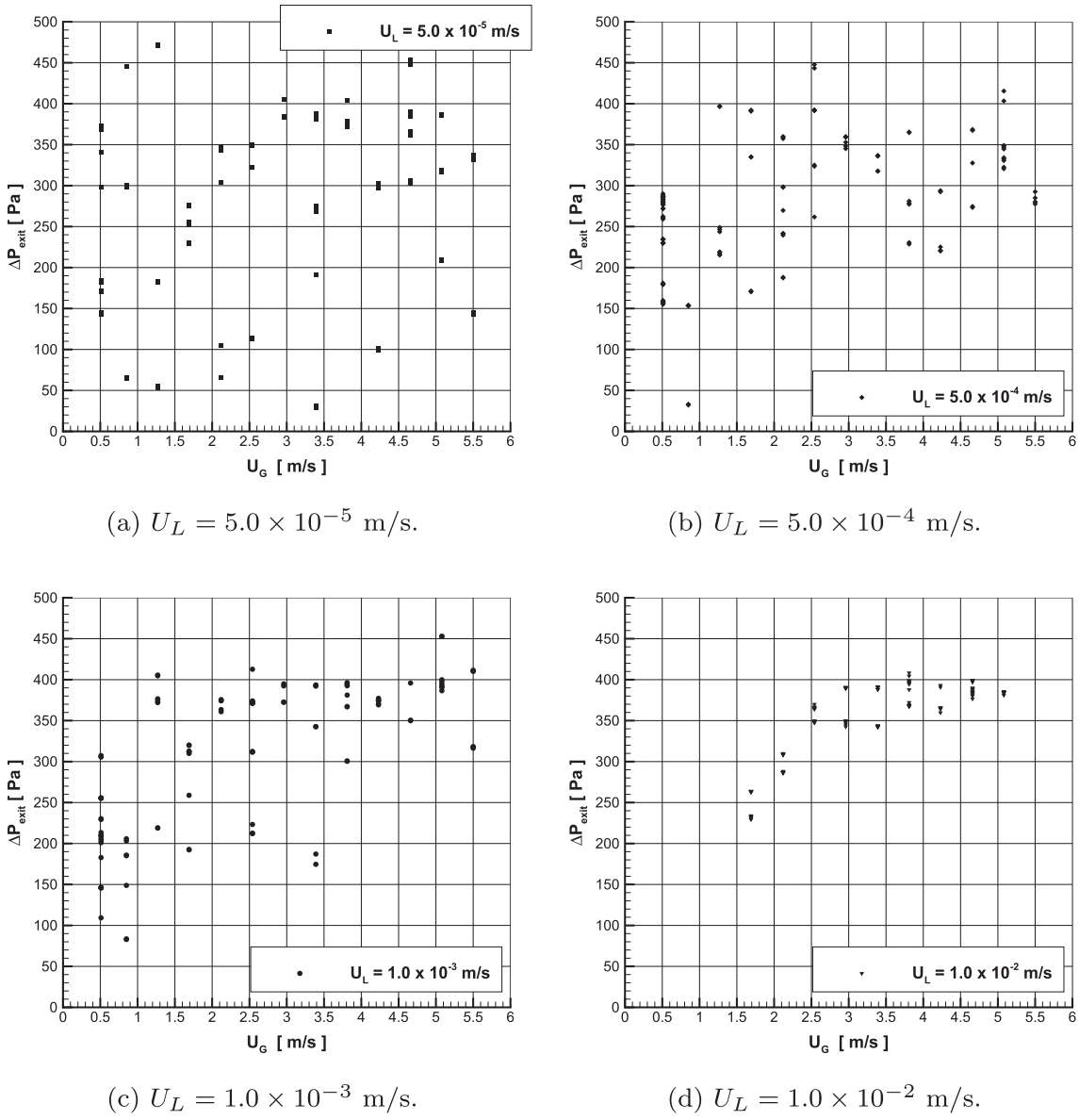

(a) $U_L = 5.0 \times 10^{-5}$ m/s.

(b) $U_L = 5.0 \times 10^{-4}$ m/s.

(c) $U_L = 1.0 \times 10^{-3}$ m/s.

(d) $U_L = 1.0 \times 10^{-2}$ m/s.

Fig. 12 – Pressure increase resulting from the exit.

reaching Tap 3 due the behavior of the water at the edge of the manifold (Figs. 10 and 11) and the flow changing direction in the form of a 90° bend. A 90° bend itself carries a pressure loss that the sudden expansion alone cannot account for.

Comparison of 90 degree bend models to the experimental data

Section 3.6 considered the pressure loss in this work as a pure sudden expansion. However, the sudden expansion in this work also includes the flow turning 90°, necessitating further analysis. Subsection 1.2 introduced several models for the pressure change resulting from a 90° bend. The use of the models relies on the determination of the resistance coefficient (κ) for single-phase flow. Based on the single-phase measurements across the channel exit and subtracting the sudden expansion loss as determined by Eq. (4) corrected by 20%, κ generally decreases from 12.5 to 1.3 as the superficial gas velocity increases from 0.51 m/s to 5.5 m/s. The results follow the trend presented by Maharudrayya et al. [60].

Determining $\Delta P_{b,tp}$ from the selected models shows the model of Paliwoda [51] produces the largest pressure loss and compares to the experimental data (Fig. 14) with a mean absolute percent error of 81%. The models of Chisholm [50] and Sookprasong [54] produce smaller values, respectively. The model of Kuhn & Morris [53] breaks down at the lowest liquid velocity due to the inverse relationship of the model to $(1-\chi)^2$. This causes the model of Kuhn & Morris to predict impossibly large pressure losses at the lowest superficial velocity. Similar to the sudden expansion analysis, the relations determining $\Delta P_{b,tp}$ cannot predict the experimental measurements.

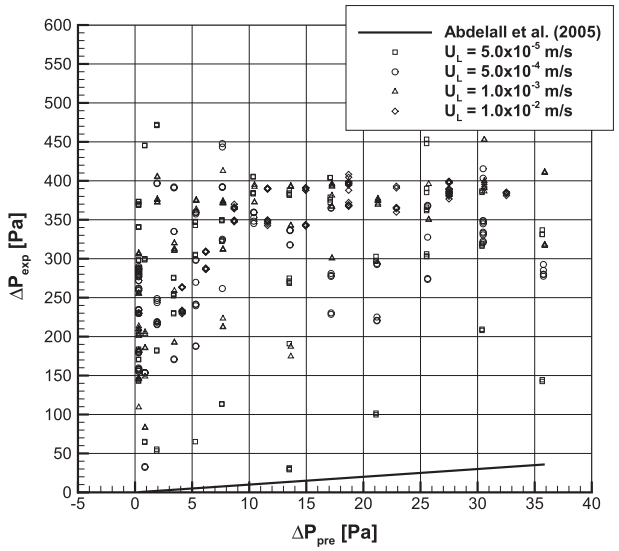

Fig. 13 – Comparison of the measured ΔP_{exit} to the prediction of Abdelall et al. [37].

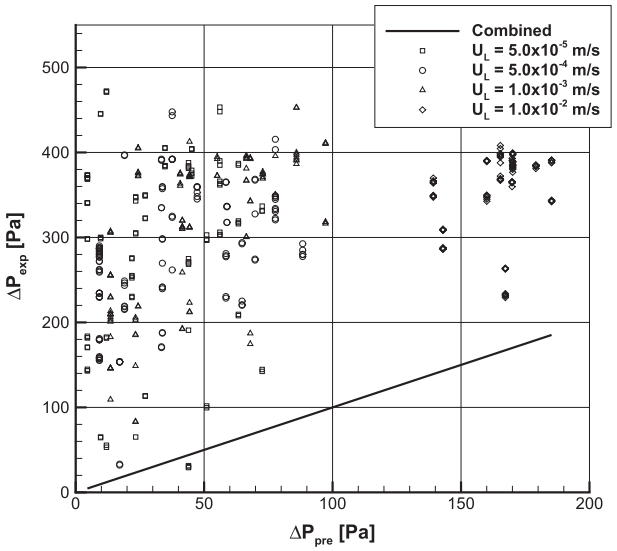

Fig. 15 – Comparison of the measured ΔP_{exit} to the combined predictions of Abdelall et al. [37] and Paliwoda [51].

Combined influence of the sudden expansion and the 90° bend

As neither the models determined for a sudden expansion nor the models for a 90° bend account for the measured pressure loss, this section will focus on the combined prediction of both mechanisms. The combination of the models of Abdelall and Paliwoda produces a mean absolute percent error of 78% (Fig. 15).

Thus, the combination of a sudden expansion and a 90° bend may account for a fraction of the measured pressure loss but the combination of the selected models cannot predict the total pressure loss. Therefore, measurements of the two-phase frictional pressure drop across a geometric change is not recommended, as it remains unclear how to predict the pressure loss resulting from the channel expanding to a manifold, preventing the isolation of the two-phase frictional pressure drop. Furthermore, the combination of the sudden expansion with the 90° bend convolutes the influence of either on the measurement.

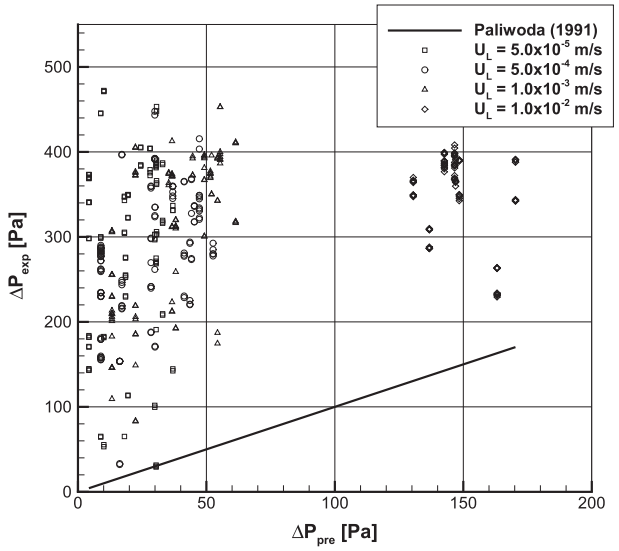

Fig. 14 – Comparison of the measured ΔP_{exit} to the prediction of Paliwoda [51].

Conclusion

This work conducted an experimental study of the pressure loss associated with air-water two-phase flow across an exit of a microchannel to a larger exit manifold. The microchannel has dimensions 3.23 mm wide by 0.304 mm high by 164 mm long and exits into a circular manifold of 1.4 cm diameter oriented 90° relative to the flow direction. The major results include:

1. The majority of the exit pressure loss data fall between 150 Pa and 400 Pa with a slight dependence on superficial gas velocity but independent of the superficial liquid velocities.
2. In general, a longer channel should mask the influence of the exit pressure loss.
3. Treating the exit as a sudden expansion and comparing the results to models for the pressure loss associated with a sudden expansion reveals a need for further refinement as the best sudden expansion model (Eq. (33)) produced a mean absolute percent error of 96%.
4. Neglecting the sudden expansion to analyze the influence of the 90° bend revealed the selected predictions cannot predict the exit pressure loss, where the best 90° bend model (Eq. (46)) produced a mean absolute percent error of 81%.
5. Combining both the sudden expansion model of Abdelall et al. and the 90° relation of Paliwoda results in a mean

absolute percent error of 78% relative to the experimental measurement of the pressure loss across the exit.

Acknowledgements

The authors gratefully acknowledge UCI's machinist, Ted Ediss, for his advice in machining the microchannel assembly. In addition, the authors thank Professor William A. Sirignano, Professor John C. LaRue, Dr. Alejandro Puga, and Dr. Tuan Minh Nguyen for their insightful discussions. Y. Wang thanks the Shanghai Everpower Technologies Ltd. for their partial financial support in PEM fuel cell research.

REFERENCES

[1] McAdams W, Woods W, Heroman Jr I. Vaporization inside horizontal tubes–ii benzene-oil mixtures. Transactions of the A.S.M.E. 1942;64(1):193–200.
[2] Cicchitti A, Lombardi C, Silvestri M, Soldaini G, Zavattarelli R. Two-phase cooling experiments: pressure drop, heat transfer and burnout measurements. Energ Nucl 1960;7(6):407–25.
[3] Lin S, Kwok C, Li R-Y, Chen Z-H, Chen Z-Y. Local frictional pressure drop during vaporization of r-12 through capillary tubes. Int J Multiphas Flow 1991;17(1):95–102. https://doi.org/10.1016/0301-9322(91)90072-B.
[4] Fourar M, Bories S. Experimental study of air-water two-phase flow through a fracture (narrow channel). Int J Multiphas Flow 1995;21(4):621–37. https://doi.org/10.1016/0301-9322(95)00005-I.
[5] Beattie D, Whalley P. A simple two-phase frictional pressure drop calculation method. Int J Multiphas Flow 1982;8(1):83–7. https://doi.org/10.1016/0301-9322(82)90009-X.
[6] Awad M, Muzychka Y. Effective property models for homogeneous two-phase flows. Exp Therm Fluid Sci 2008;33(1):106–13. https://doi.org/10.1016/j.expthermflusci.2008.07.006.
[7] Lockhart R, Martinelli R. Proposed correlation of data for isothermal two-phase, two-component flow in pipes. Chem Eng Prog 1949;45:39–48.
[8] Chisholm D. A theoretical basis for the lockhart-martinelli correlation for two-phase flow. Int J Heat Mass Tran 1967;10(12):1767–78. https://doi.org/10.1016/0017-9310(67)90047-6.
[9] Mishima K, Hibiki T. Some characteristics of air-water two-phase flow in small diameter vertical tubes. Int J Multiphas Flow 1996;22(4):703–12. https://doi.org/10.1016/0301-9322(96)00010-9.
[10] Zhang W, Hibiki T, Mishima K. Correlations of two-phase frictional pressure drop and void fraction in mini-channel. Int J Heat Mass Tran 2010;53(1):453–65. https://doi.org/10.1016/j.ijheatmasstransfer.2009.09.011.
[11] English NJ, Kandlikar SG. An experimental investigation into the effect of surfactants on air-water two-phase flow in minichannels. Heat Tran Eng 2006;27(4):99–109. https://doi.org/10.1080/01457630500523980.
[12] Li W, Wu Z. A general correlation for adiabatic two-phase pressure drop in micro/mini-channels. Int J Heat Mass Tran 2010;53(13):2732–9. https://doi.org/10.1016/j.ijheatmasstransfer.2010.02.029.
[13] Sun L, Mishima K. Evaluation analysis of prediction methods for two-phase flow pressure drop in mini-channels. Int J Multiphas Flow 2009;35(1):47–54. https://doi.org/10.1016/j.ijmultiphaseflow.2008.08.003.
[14] Ma Y, Ji X, Wang D, Fu T, Zhu C. Measurement and correlation of pressure drop for gas-liquid two-phase flow in rectangular microchannels. Chin J Chem Eng 2010;18(6):940–7. https://doi.org/10.1016/S1004-9541(09)60151-8.
[15] Kim S-M, Mudawar I. Universal approach to predicting two-phase frictional pressure drop for adiabatic and condensing mini/micro-channel flows. Int J Heat Mass Tran 2012;55(11):3246–61. https://doi.org/10.1016/j.ijheatmasstransfer.2012.02.047.
[16] Li X, Hibiki T. Frictional pressure drop correlation for two-phase flows in mini and micro single-channels. Int J Multiphas Flow 2017;90(Suppl C):29–45. https://doi.org/10.1016/j.ijmultiphaseflow.2016.12.003.
[17] Lee HJ, Lee SY. Pressure drop correlations for two-phase flow within horizontal rectangular channels with small heights. Int J Multiphas Flow 2001;27(5):783–96. https://doi.org/10.1016/S0301-9322(00)00050-1.
[18] Saisorn S, Wongwises S. The effects of channel diameter on flow pattern, void fraction and pressure drop of two-phase airwater flow in circular micro-channels. Exp Therm Fluid Sci 2010;34(4):454–62. https://doi.org/10.1016/j.expthermflusci.2009.02.006.
[19] Corey A. The interrelation between gas and oil relative premeabilities. Prod Mon 1954;19:38–41.
[20] Nowamooz A, Radilla G, Fourar M. Non-darcian two-phase flow in a transparent replica of a rough-walled rock fracture. Water Resour Res 2009;45(7):1–9. https://doi.org/10.1029/2008WR007315.
[21] Chen C-Y, Horne RN, Fourar M. Experimental study of liquid-gas flow structure effects on relative permeabilities in a fracture. Water Resour Res 2004;40(8):1–15. https://doi.org/10.1029/2004WR003026.
[22] Fourar M, Lenormand R. A viscous coupling model for relative permeabilities in a fracture, SPE Annual Technical Conference and Exhibition, September 27–30. Society of Petroleum Engineers; 1998. https://doi.org/10.2118/49006-MS.
[23] Huang H, Li Z, Liu S, Lu X-y. Shan-and-chen-type multiphase lattice Boltzmann study of viscous coupling effects for two-phase flow in porous media. Int J Numer Meth Fluid 2009;61(3):341–54. https://doi.org/10.1002/fld.1972.
[24] Wang Y. Porous-media flow fields for polymer electrolyte fuel cells ii. analysis of channel two-phase flow. J Electrochem Soc 2009;156:B1134–41. https://doi.org/10.1149/1.3183785.
[25] Qu W, Mudawar I. Flow boiling heat transfer in two-phase micro-channel heat sinksi. experimental investigation and assessment of correlation methods. Int J Heat Mass Tran 2003;46(15):2755–71. https://doi.org/10.1016/S0017-9310(03)00041-3.
[26] Thiangtham P, Keepaiboon C, Kiatpachai P, Asirvatham LG, Mahian O, Dalkilic AS, et al. An experimental study on two-phase flow patterns and heat transfer characteristics during boiling of r134a flowing through a multi-microchannel heat sink. Int J Heat Mass Tran 2016;98:390–400. https://doi.org/10.1016/j.ijheatmasstransfer.2016.02.051.
[27] Lee J, Mudawar I. Two-phase flow in high-heat-flux micro-channel heat sink for refrigeration cooling applications: Part ii heat transfer characteristics. Int J Heat Mass Tran 2005;48(5):941–55. https://doi.org/10.1016/j.ijheatmasstransfer.2004.09.019.
[28] Col DD, Bortolin S. Investigation of dryout during flow boiling in a single microchannel under non-uniform axial heat flux. Int J Therm Sci 2012;57:25–36. https://doi.org/10.1016/j.ijthermalsci.2012.01.020.
[29] Li X, Sabir I. Review of bipolar plates in pem fuel cells: flow-field designs. Int J Hydrogen Energy 2005;30(4):359–71. https://doi.org/10.1016/j.ijhydene.2004.09.019.

[30] Wang Y, Basu S, Wang C-Y. Modeling two-phase flow in pem fuel cell channels. J Power Sources 2008;179(2):603–17. https://doi.org/10.1016/j.jpowsour.2008.01.047.
[31] Adroher XC, Wang Y. Ex situ and modeling study of two-phase flow in a single channel of polymer electrolyte membrane fuel cells. J Power Sources 2011;196(22):9544–51. https://doi.org/10.1016/j.jpowsour.2011.07.076.
[32] Lu Z, Kandlikar S, Rath C, Grimm M, Domigan W, White A, et al. Water management studies in pem fuel cells, part ii: ex situ investigation of flow maldistribution, pressure drop and two-phase flow pattern in gas channels. Int J Hydrogen Energy 2009;34(8):3445–56. https://doi.org/10.1016/j.ijhydene.2008.12.025.
[33] Konno N, Mizuno S, Nakaji H, Ishikawa Y. Development of compact and high-performance fuel cell stack. SAE Int J Altern Powertrains 2015;4(1):123–9. https://doi.org/10.4271/2015-01-1175.
[34] Grimm M, See EJ, Kandlikar SG. Modeling gas flow in pemfc channels: part i flow pattern transitions and pressure drop in a simulated ex situ channel with uniform water injection through the gdl. Int J Hydrogen Energy 2012;37(17):12489–503. https://doi.org/10.1016/j.ijhydene.2012.06.001.
[35] Phan HT, Caney N, Marty P, Colasson S, Gavillet J. Flow boiling of water in a minichannel: the effects of surface wettability on two-phase pressure drop. Appl Therm Eng 2011;31(11):1894–905. https://doi.org/10.1016/j.applthermaleng.2011.02.036.
[36] Effect of taper on pressure recovery during flow boiling in open microchannels with manifold using homogeneous flow model. Int J Heat Mass Tran 2015;83:109–17.
[37] Abdelall F, Hahn G, Ghiaasiaan S, Abdel-Khalik S, Jeter S, Yoda M, et al. Pressure drop caused by abrupt flow area changes in small channels. Exp Therm Fluid Sci 2005;29(4):425–34. https://doi.org/10.1016/j.expthermflusci.2004.05.001.
[38] Delhaye J. Singular pressure drops. In: Bergles A, editor. Two-phase flow and heat transfer in the power and process industries. 1st ed. Hemisphere Publishing Corporation; 1981. p. 124–50. Ch. 4.
[39] Romie F. Private communication with P.A. Lottes. 1958.
[40] Lottes P. Expansion losses in two-phase flow. Nucl Sci Eng 1961;9(1):26–31.
[41] Collier J, Thome J. Convective boiling and condensation. 3rd ed. Clarendon Press; 1996.
[42] Richardson BL. Some problems in horizontal, two-phase two-component flow. Ph.D. thesis. Purdue University; 1958.
[43] Attou A, Bolle L. A new correlation for the two-phase pressure recovery downstream from a sudden enlargement. Chem Eng Technol 1997;20(6):419–23. https://doi.org/10.1002/ceat.270200610.
[44] Rouhani Z. Modified correlations for void and two-phase pressure drop, Report AE-RTV-841. 1969.
[45] Schmidt J, Friedel L. Two-phase flow pressure change across sudden expansions in duct areas. Chem Eng Commun 1996;141–142(1):175–90. https://doi.org/10.1080/00986449608936415.
[46] Chisholm D, Sutherland L. Prediction of pressure gradients in pipeline systems during two-phase flow. Proc Inst Mech Eng 1969;184(3C):24–32.
[47] Wadle M. A new formula for the pressure recovery in an abrupt diffusor. Int J Multiphas Flow 1989;15(2):241–56. https://doi.org/10.1016/0301-9322(89)90073-6.
[48] Chen IY, Wongwises S, Yang B-C, Wang C-C. Two-phase flow across small sudden expansions and contractions. Heat Tran Eng 2010;31(4):298–309. https://doi.org/10.1080/01457630903312056.
[49] Kawahara A, Chung P-Y, Kawaji M. Investigation of two-phase flow pattern, void fraction and pressure drop in a microchannel. Int J Multiphas Flow 2002;28(9):1411–35. https://doi.org/10.1016/S0301-9322(02)00037-X.
[50] Chisholm D. Two-phase flow in bends. Int J Multiphas Flow 1980;6(4):363–7. https://doi.org/10.1016/0301-9322(80)90028-2.
[51] Paliwoda A. Generalized method of pressure drop calculation across pipe components containing two-phase flow of refrigerants. Int J Refrig 1992;15(2):119–25. https://doi.org/10.1016/0140-7007(92)90036-T.
[52] Azzi A, Belaadi S, Friedel L. Two-phase gas/liquid flow pressure loss in bends. Forsch Im Ingenieurwes 1999;65(7):309. https://doi.org/10.1007/BF03035112.
[53] Kuhn H, Morris S. Private communication with Azzi et al. 1999. 1997.
[54] Sookprasong P, Brill J, Schmidt Z. Two-phase flow in piping components. ASME J Energy Resour Technol 1986;108(3):197–201. https://doi.org/10.1115/1.3231264.
[55] J. M. Lewis, Y. Wang, Two-phase frictional pressure drop and water film thickness in a thin hydrophilic microchannel, Int J Heat Mass Tran.
[56] Kakac S, Shah R, Aung W. Handbook of single-phase convective heat transfer. Wiley; 1987.
[57] Shah R, London A. Laminar flow forced convection heat transfer and flow friction in straight and curved ducts–a summary of analytical solutions. Tech. Rep. Standford University, Department of Mechanical Engineering; 11 1971.
[58] Shah R. A correlation for laminar hydrodynamic entry length solutions for circular and noncircular ducts. J Fluid Eng 1978;100:177–9. https://doi.org/10.1115/1.3448626.
[59] Zeng W, Jacobi I, Beck DJ, Li S, Stone HA. Characterization of syringe-pump-driven induced pressure fluctuations in elastic microchannels. Lab Chip 2015;15:1110–5. https://doi.org/10.1039/C4LC01347F.
[60] Maharudrayya S, Jayanti S, Deshpande A. Pressure losses in laminar flow through serpentine channels in fuel cell stacks. J Power Sources 2004;138(1):1–13. https://doi.org/10.1016/j.jpowsour.2004.06.025.